Transformative high entropy alloy conquers the strength-ductility paradigm by massive interface strengthening

S.S. Nene[1,2], P. Agrawal[2], M. Frank[2], A. Watts[2], S. Shukla[3], C. Morphew[2], A. Chesetti[2], J. S. Park[4], R.S. Mishra[2*]

[1]*Department of Metallurgical and Materials Engineering, Indian Institute of Technology Jodhpur, 342037 India*

[2]*Center for Friction Stir Processing, Department of Materials Science and Engineering, University of North Texas, Denton, Texas 76207 USA*

[3]*Oak Ridge National Laboratory, Oak Ridge, TN 37830, USA*

[4]*Advanced Photon Source, Argonne National Laboratory, Lemont, IL 60439, USA*

**Corresponding author email: rajiv.mishra@unt.edu*

Abstract

Recent metastable alloy designs have demonstrated simultaneous attainment of high ultimate tensile strength (UTS) and ductility in high entropy alloys but with low yield strength. Here we present new strategy for improving the work hardenability and yield strength (YS) together in $Fe_{38.5}Mn_{20}Co_{20}Cr_{15}Si_5Cu_{1.5}$ high entropy alloy (Cu-HEA). Drastic increase in the YS (1.5 GPa) is attributed to the formation of γ/ε, ε/ε (twin type) and ε/ε (plate type) interfaces in the microstructure due to extreme grain refinement whereas high UTS-ductility synergy (2.2 GPa, 15%) is attained by dynamic Hall-Petch hardening across these interfaces (i.e. massive interface strengthening) and transformation induced plasticity in γ phase. Thus, this harmonious combination of YS and UTS-ductility synergy in Cu-HEA outperform all structural materials till date. Therefore, deformation-induced massive interface strengthening is a new, yet cost-effective pathway for synergizing the benefits of advanced steels and high entropy alloys together in a material by conventional processing route.

Key words: grain refinement, dual-phase high entropy alloy, metastability, strength-ductility paradigm, ε-h.c.p. phase

Almost a decade ago, Yeh *et al.*[1] and Cantor *et al.*[2] introduced a new alloy design strategy wherein maximizing the number of constituent elements in the alloy system will minimize the tendency of solute partitioning thereby resulting in formation of simple yet disordered solid solutions in the microstructure of the material [1,2]. They termed this new class of materials as high entropy alloys (HEAs). Recently, Li *et al.*[3] and conceptualized new class of HEAs known as metastable dual phase alloys which not only have high entropy characteristics but also exhibits transformation induced plasticity (TRIP) as an additional strengthening mechanism contributing to enhanced ductility while increasing the strength. However, Li *et al.* [3] obtained very poor yield strength in the $Fe_{50}Mn_{30}Co_{10}Cr_{10}$ HEA though it had excellent strength-ductility response. This alloy design approach opened a vast potential of engineering γ-F.C.C. phase stability in FeMnCoCr system by changing the alloy chemistry with minor additions of γ destabilizers (i.e. ε-H.C.P. stabilizers). In line with that, we designed extremely metastable HEAs by addition of Si (γ destabilizer) and Al, Cu (γ stabilizers) in FeMnCoCr system which showed propensity of obtaining multiple deformation mechanisms during room temperature deformation [4-8]. It was thought that simultaneous addition of Cu and Si into FeMnCoCr system not only makes the γ phase metastable but also increases its deformation storage capacity (DSC) before it transforms to ε phase on straining which we termed as controlled metastability (γ phase can deform by dislocation activity before it transforms to ε phase) of γ phase [6-8]. We investigated $Fe_{38.5}Mn_{20}Co_{20}Cr_{15}Si_{5}Cu_{1.5}$ HEA (henceforth designated as Cu-HEA) to realize controlled metastability and effect of this controlled metastability on microstructural evolution and resultant deformation response in conventionally rolled Cu-HEA.

The $Fe_{38.5}Mn_{20}Co_{20}Cr_{15}Si_{5}Cu_{1.5}$ (all in atomic %) was received from Sophisticated alloys in the form of rolled sheets with a final thickness of 6.5 mm and 3.15 mm, respectively. They fabricated the alloy by the conventional induction melting and the starting thickness of the ingot for the rolling was ~35 mm. After homogenization at 900 °C for 2 hrs, the ingot then was subjected to hot rolling at 900 °C to reach to a thickness of 6.5 mm (R_1 condition). The rolled plate then was cut in half, descaled and reheated to 500 °C and rolled to the final thickness of 3.15 mm (R_2 condition). A piece was cut from this warm rolled plate and subjected to cold rolling using hot rolling mill set-up manufactured by the International Rolling Mill Ltd. to the final thickness of 2.03 mm (R_3 condition) at the UNT rolling facility. Four rolling passes were made in R_3 condition to reach to the final thickness (2.03 mm) without intermediate reheating of specimens.

The microstructure of the alloy in thermo-mechanically processed conditions was analyzed at different length scales. Nano-Scanning electron microscope (SEM) with a Hikari Super electron backscattered diffraction (EBSD) detector was used to investigate the phase fraction at micron level for as-rolled sample for R_1 and R_2 conditions and TSL OIM8 software was used for analysis. The R_3 condition samples in undeformed and deformed conditions were taken for ex-situ Synchrotron (high energy X-ray) experiments at 1-ID-E beamline of the Advanced Photon Source, Argonne National Laboratory, and transmission electron microscope (TEM) at Materials Research Facility (MRF), UNT Denton. For Synchrotron experiments the wavelength used was 0.17296 $\dot{A}$ where single shots were taken with an exposure time of 1.7s. A dark file with the same parameters was acquired to remove the background from the data obtained. The synchrotron data is presented in the form of Debye rings and intensity vs 2θ plots to present the evolution of phases. The data is analyzed using the General Structure Analysis System-II (GSAS-II) software. TEM microscopy was carried out on FEI Tecnai G2 F20 S-Twin 200keV FE-STEM where the samples were milled with FEI Nova 200 NanoLab Dual Beam Focused Ion Beam (FIB)/ Field Emission Scanning Electron Microscope (FE-SEM) with platinum gun injection system (Pt GIS). Precession electron diffraction (PED) [9], TEM based OIM was carried out to obtain the phase fraction for the R_3 condition along with the orientation information. TOPSPIN software was used for the acquisition of the PED data with ASTAR hardware from NanoMEGAS.

Rectangular 1 mm-thick, dog-bone-shaped mini-tensile specimens were machined using a mini computer numerical control (CNC) machine from the rolled sheet in the transverse direction. Gage length and width of the tensile specimens were ∼5 and ∼1.25 mm, respectively. In each condition, three samples were tested at room temperature and initial strain rate of 10^{-3} s^{-1} to confirm the reproducibility of the results.

Figure 1 (a) shows the overall schematic of the thermo-mechanical processing schedule used for Cu-HEA. The rolling temperatures for each step were selected such that it is well above the $\gamma \rightarrow \varepsilon$ and $\gamma \rightarrow \sigma$ transformation temperatures for Cu-HEA to obtain γ dominated microstructure after warm rolling [8-9]. As expected, microstructure was significantly refined because of the temperature drop in each rolling step while retaining the high volume fraction of γ in the microstructure (Figs. 1(b-d)). The last step of rolling at room temperature, however, imparted heavy deformation induced transformation resulting in an extremely refined microstructure with ~50:50 distribution of γ and ε phases (Fig. 1 (d)). Detailed investigation of microstructure in R_3 specimen by TEM provided very interesting observations regarding co-existence of γ/γ, γ/ε, ε/ε (plate) and ε/ε (twins) interfaces. Formation of such multiple interfaces in the microstructure due to extreme grain refinement as a result of imposed thermomechanical processing give rise to ***massively interfaced microstructure***. Fig. 2 (a) shows the overall bright field image of the R_3 specimen after rolling at room temperature (RT) displaying massively interfaced region. To identify the type of the interfaces, precession electron diffraction (PED) scans were obtained from the selected region of Fig. 2 (a, highlighted by the red box) which is shown in the Fig. 2 (b).

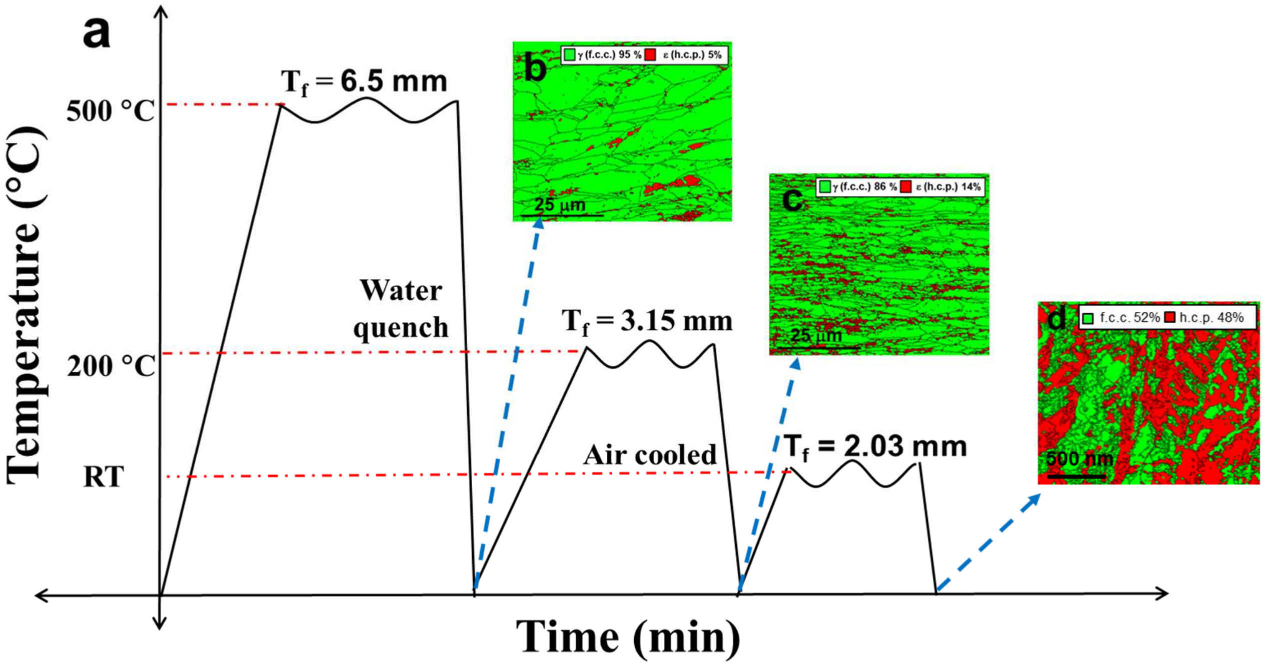

Fig. 1. Thermo-mechanical processing of Cu-HEA. (a) A schematic of overall processing, (b) EBSD phase map of R_1 specimen, (c) EBSD phase map of R_2 specimen, and (d) PED phase map of R_3 specimen. (EBSD: Electron back scattered diffraction, PED: precession electron diffraction, HEA: high entropy alloy)

PED phase maps in Figs. 2 (b-b_1) display the γ/γ interface highlighted with black arrows whereas PED phase map in the Figs. 2 (c,d) highlight the γ/ε interfaces. Detail misorientation analysis at γ/ε (Fig. 2 (b_2)) suggest that formation of ε phase (as a result of TRIP effect) is prevalent in grains which exhibit Shoji-Nishiyama (SN) type of orientation relationship (OR) denoted by $(111)\gamma \parallel (0001)\varepsilon$ and $(10\bar{1})\gamma \parallel (11\bar{2}0)\varepsilon$. This finding in present work is consistent with results on Mn containing TRIP steel by Herrera *et al.* [10] and our recent study on Al-HEA [6,8]. It was further noted that, ε phase forms in two different variants which give rise to two distinct interfaces, one with very low misorientation (ε/ε-plate) and the other with higher misorientation (ε/ε-twin) [7,8,11].

Conventional bright field transmission electron microscopy (BF-TEM) imaging along with the PED phase map in Figs. 2 (c,c_1,c_2) confirm the formation of ε twins which is further supported by the 58-60° misorientation between the parent grains and the twin pointing towards the formation of classic h.c.p. $\{10\bar{1}1\}$ contraction twins [8,11] (Figs. 2(c_3,c_4)) after cold rolling in Cu-HEA. On a similar note, BF-TEM imaging and PED phase map in Figs. 2 (d,d_1) display the formation of ε plates and is supported by very marginal misorientation (~2°) among the plates in PED inverse pole figure map (Fig. 2 (d_2,d_3)).

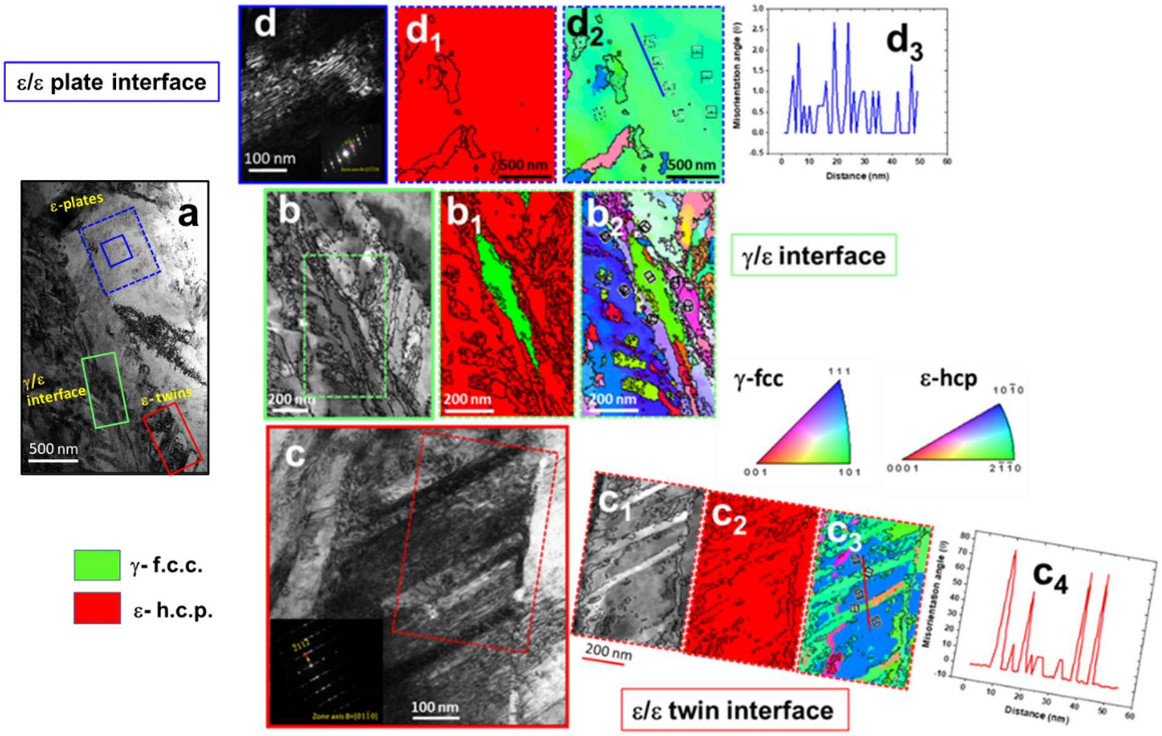

Fig. 2: Massively-interfaced microstructure in Cu-HEA. (a) BF-TEM image showing overall microstructure of R_3 specimen, (b) PED back scattered map, (b_1) phase and (b_2) IPF map showing γ/ε interfaces, (c) BF-TEM image and corresponding SAD pattern, (c_1) PED backscattered map, (c_2) PED phase map and (c_3) IPF map showing ε/ε twin interfaces, (c_4)

Misorientation analysis for ε/ε twin interfaces (d) BF-TEM image and corresponding SAD pattern (d_1) PED phase map and (d_2) IPF map showing ε/ε plate interfaces, (d_3) Misorientation analysis for ε/ε plate interfaces. (TEM: Transmission electron microscopy, BF: bright field; PED: precession electron diffraction, IPF: inverse pole figure; HEA: high entropy alloy; SAD: selected area diffraction)

The uniqueness of the microstructure not only lies in the higher number of interfaces but also their extremely fine size attained after the thermo-mechanical processing as shown in Figs. 2 (c,d) for ε-twins (~20-30 nm) and ε-plates (~15-25 nm), respectively. Moreover, the fraction and distribution of these different interfaces in the microstructure contribute significantly in controlling the deformation behavior of the material. It is seen that, the formation of either twins or plates is governed by the c/a ratio of the ε phase formed in the metastable HEAs [8,11,12]. Additionally, our earlier results showed that TRIP-assisted HEAs exhibit a concurrent decrease in the c/a ratio of ε phase resulting in synergistic activation of twinning and plate formation during deformation. However, Cu-HEA being relatively stable compared to other compositional variants namely $Fe_{40}Mn_{20}Co_{20}Cr_{15}Si_5$ HEA (CS-HEA) [5,8] and $Fe_{39}Mn_{20}Co_{20}Cr_{15}Si_5Al_1$ (Al-HEA) [6,8], it should not exhibit responsive evolution in c/a ratio of the ε phase during deformation. Indeed, c/a ratio measurement of the ε phase in R_3 specimen by XRD showed stable nature of c/a ratio in the current Cu-HEA and marginal drop in the c/a value from 1.6323 to 1.6283 after complete tensile deformation (evaluated from XRD data not shown here). As concurrent drop in c/a ratio is an indication of pronounced participation of non-basal activities in stain accommodation by ε phase, R_3 specimen lacks it due to more rigid nature of c/a ratio [8,11]. As a result, activation of non-basal activities become sluggish which prefers formation of ε-twins over ε-plates in Cu-HEA. Hence detailed investigation of rolled Cu-HEA microstructure displayed higher fraction of ε twinned regions than ε plates containing areas. The deformation response of this heavily interfaced microstructure was studied in detail and has been correlated with the microstructural features in subsequent discussion.

Figure 3 (a) shows the engineering stress-engineering strain curves for R_1, R_2 and R_3 specimens. At different stages during processing (i.e. R_1, R_2 and R_3 conditions), the material exhibited dramatically different tensile responses as shown in Fig. 3 (a). The specimen exhibiting massively-interfaced microstructure (R_3, blue curve in Fig. 3 (a)) displayed highest yield strength

(YS) of 1.5 GPa and ultimate tensile strength (UTS) of 1.95 GPa (true UTS of 2.2 GPa) in comparison with the R_1 (805 MPa, 1.0 GPa) and R_2 (1.12 GPa, 1.29 GPa) specimens after complete tensile deformation. The interesting observation is ~ 85% increase in YS in comparison with the R_1 specimen but with controlled drop in ductility (by ~ 40%).

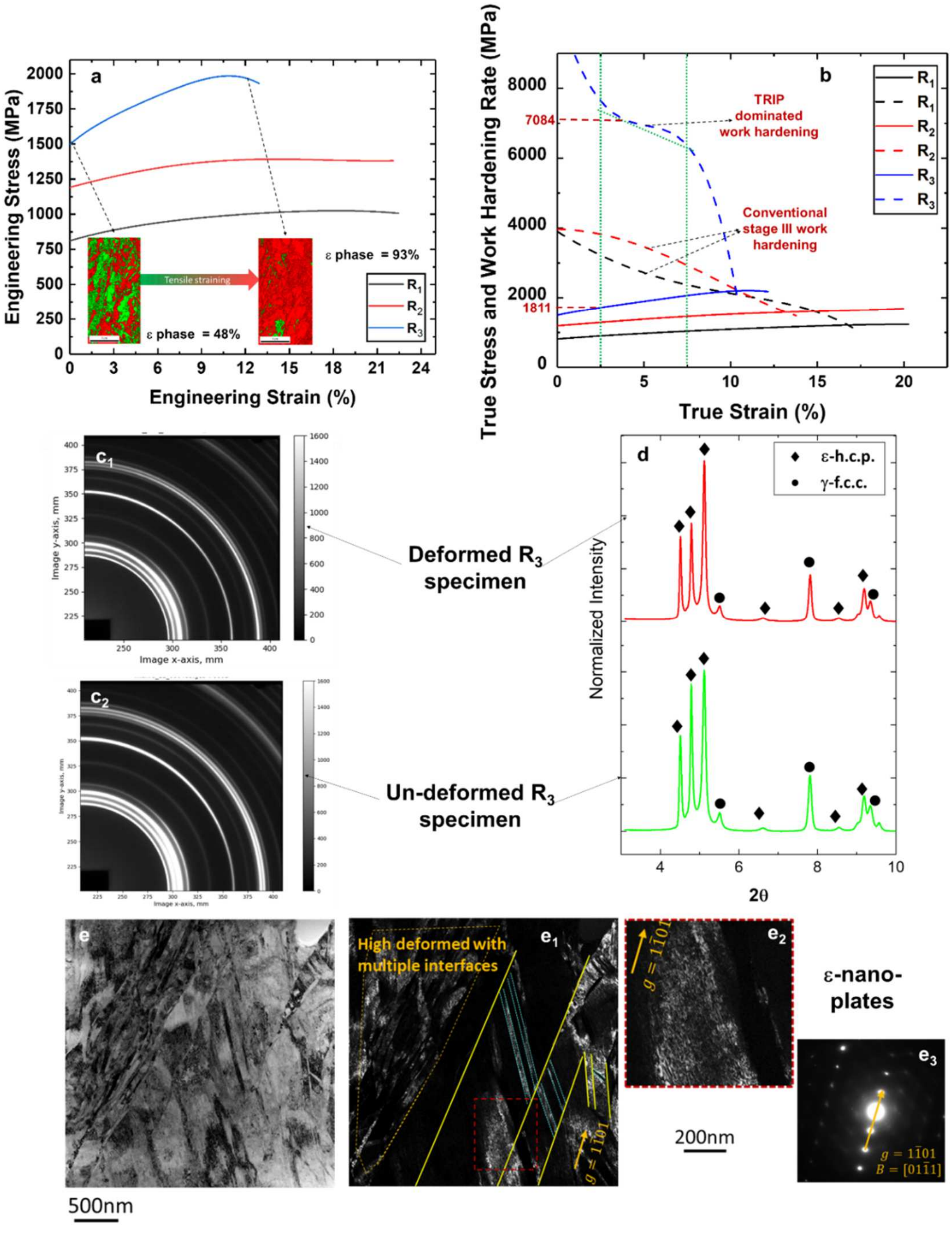

Fig. 3. Tensile properties of Cu-HEA. (a) Engineering stress- engineering strain curves for Cu-HEA in all conditions, (b) work hardening curves and true stress- true strain curves for Cu-HEA

in all conditions. High energy X-ray synchrotron results for R_3 specimen. (c) Debye rings for (c_1) deformed, (c_2) undeformed, and (d) intensity vs. 2theta plots for undeformed and deformed samples, (e) bright field TEM image showing deformed microstructure for R_3 specimen, (e_1) dark field image corresponding to Fig. 3e marked with ε-twins and plates, (e_2, e_3) high magnification bright field TEM image showing ε-nano plates with respective SAD pattern. (HEA: high entropy alloy, TEM: Transmission electron microscopy, SAD: selected area diffraction)

Fig. 3 (b) highlights the work hardening (WH) response of these specimens along with the corresponding true stress-true plastic strain curves suggesting the strain accommodation mechanisms in them. It is clear that R_3 specimen displayed significantly different WH response (blue dotted curve in Fig. 3 (b)) other than the conventional stage III (dislocation dominated) strain accommodation shown by R_1 and R_2 specimens (red and block dotted curves shown in Fig. 3(b)). The onset of change in slope marked in the dotted blue WH curve point towards activation of additional deformation mechanism in R_3 specimen for strain accommodation. The notable observation is the change in the slope of WH curve at a very high WH rate of 7084 MPa which is very unconventional and hard to attain in conventional materials. The detail analysis of the microstructure by PED and X-ray synchrotron for the same specimen showed evidence of $\gamma \rightarrow \varepsilon$ transformation after tensile deformation suggesting TRIP to be one of the primary mode for deformation in the material (inset of Fig. 3 (a) and Figs. 3 (c_1,c_2,d)). On the similar lines, the WH rate was sustained at the value of 7084 MPa over a strain range of 2.5 to 7.5 % and corresponds to a true stress of 1.81 GPa as shown by the green dotted line markings in Fig. 3 (b). This sustainment of WH over the above mentioned strain levels also supports operation of TRIP as strain accommodation mechanism at the stress value of 1.81 GPa (TRIP stress). This value of TRIP stress is highest in comparison with the TRIP stress values reported for TRIP steels and HEAs till date [6-8, 11-12] and indicates that the activation of TRIP got delayed till 1.81 GPa in R_3 specimen which can be attributed to following primary considerations:

1. Heavily interfaced microstructure created by the thermo-mechanical processing as a result of extreme grain refinement has pushed the yield strength to over 1 GPa. This dramatic jump in the yield strength is attributed to the decrease in the mean free path for the dislocation motion during subsequent tensile deformation as a result of nano-sized multiple interfaces in the microstructure [8,13-16] (Fig. 4 (a)).

2. Due to controlled metastability in Cu-HEA, the deformation storage capacity (ability to create and hinder dislocations at γ phase) has increased which resulted in deformation from 1.5 GPa till 1.8 GPa without activation of TRIP [1, 6-8,11-17].
3. Also, very fine grain size and higher fraction of ε phase prior to tensile deformation exerts a back stress at the pre-existing γ/ε interfaces resulting in further delaying TRIP activation [1,6-8 , 17-21].

As TRIP takes over after 1.81 GPa, deformation gets accommodated from 2.5 to 7.5 % beyond which the WH rate found to decrease and material moves back to stage III of work hardening during deformation (Fig. 3 (b)). However, material is still able to deform with substantial WH (Figs. 3 (a,b)) which is mainly associated with the dynamic Hall-Petch hardening induced by the pre-existing massive interfaces and also by newly created ε/ε interfaces (as a result of TRIP, Figs. 3 (e-e_3)) reaching to overall ductility of 15% while maintaining ultra-high strength of 2.2 GPa [8, 11, 15-20]. As a result, strain accommodation beyond 7.5% till 15% at stress levels of > 1.9 GPa in R_3 specimen is a result of dislocation accommodation at the numerous interfacial barriers retaining the WH ability of the material. Thus, this retention of WH ability in the material at such a high stress levels can be defined as interface induced plasticity which is very difficult to activate in conventional materials due to absence of such massive presence of nano interfaces [8,11,20]. Also, there will be some plastic deformation associated with pre-existing and newly formed ε phase but will be limited due to its higher c/a ratio in Cu-HEA [8, 11, 20]. In short, multiple deformation modes activated over the period of time during tensile deformation such as slip-assisted plasticity, TRIP and interface-induced plasticity provided a very high strength-ductility synergy for R_3 specimen even after yielding at very high stress of 1.5 GPa. As a result, formation of variety of interfaces played a crucial role in conquering the traditional strength-ductility paradigm even though after reaching to YS in GPa domain.

Figure 4 (b) captures the overall strength-ductility synergy in all advanced high strength materials like steels and HEAs in the form of work hardening ability (strength-ductility index, SDI = (UTS-YS)*ductility) and the corresponding UTS values. It is clearly shown by the red filled circle marked in Fig. 4 (b) that, Cu-HEA outperforms all existing advanced high strength materials in strength-ductility synergy. It further opens new SDI-UTS domain which was never explored due to inability of all pre-exiting materials to reach to such a high strength-ductility synergy at room temperature. Figure 4 (b) also points out that, the advanced high strength steels like deformed and partitioned TRIP steel [22] could not show work hardening ability when UTS reached to 2.1 GPa thereby limiting its ductility at room temperature.

In short, our effort showed that, conventional thought of tuning the grain size and phase fractions alone does not help in attaining higher strength-ductility synergy in metastable HEAs as reported by earlier studies [1-8]. However as emphasized here, the alloy design and processing path in the current study is different in approach to that reported in the pioneering metastable alloy design work earlier in HEAs [1,4-8]. Balancing the deformation storage capacity and TRIP effect in the material can lead to formation of massively interfaced microstructure than can synergistically activate multiple deformation mechanisms during straining which is otherwise difficult to achieve in any material at room temperature.

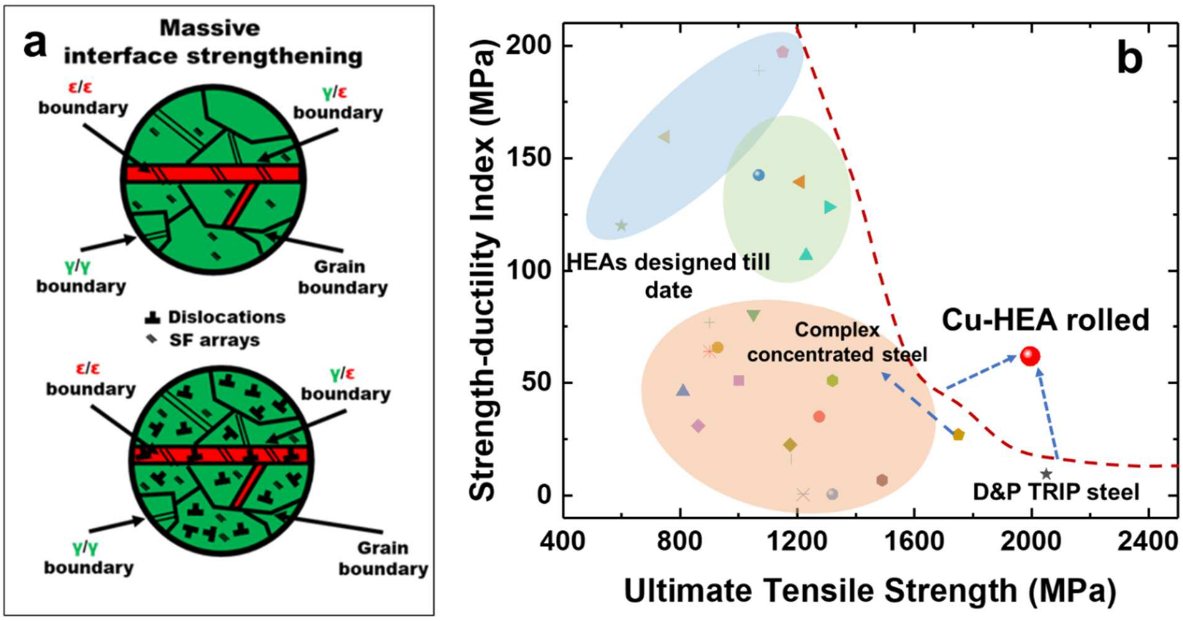

Fig. 4. (a) Schematic showing massive interface strengthening in Cu-HEA, and (b) strength-ductility index vs UTS plot for all advanced high strength steels and HEAs [5-7,22-41]. (HEA: high entropy alloy)

Acknowledgments

The work was performed under a cooperative agreement between the Army Research Laboratory and the University of North Texas (W911NF-18-2-0067). The authors are thankful to the

Materials Research Facility (MRF) for providing access to the microscopy facilities at the University of North Texas. The synchrotron experiments were carried out with awarded beam time with Proposal ID: 67642 at Advanced Photon Source, Argonne National Laboratory, USA. The authors thank Dr. Jun-Sang Park, Dr. Jonathan Almer, and Dr. Ali Mashayekhi with the proposal and onboarding process during scheduled beam time.

Author Contributions

S.S.N. and R.S.M. designed the research; S.S.N., A.W. processed and characterized the alloy; P.A. performed TEM and X-Ray synchrotron experiments; S.S. performed sample preparation for TEM; J.S.P. helped in performing X-ray synchrotron experiments and respective data analysis; S.S.N., M.F., P.A. and R.S.M. analyzed the results; S.S.N. and R.S.M. drafted the manuscript. All authors discussed the results and contributed to the final manuscript.

Competing financial interests: The authors declare no competing financial interests.

Data Availability: The raw/processed data required to reproduce these findings cannot be shared at this time as the data also forms part of an ongoing study.

References

1. J.W. Yeh, S.K. Chen, S. Lin, J.Y. Gan, T.S. Chin, T.T. Shun, C.H. Tsau, S.Y. Chang, *Adv. Eng. Mater.* **6** (2004) 299 - 303.
2. B. Cantor, B. Cantor, I.T.H. Chang, P. Knight, A.J.B. Vincent *et al., Nature* **534** (2016) 227 - 230.
3. Z. Li, K.G. Pradeep, Y. Deng, D. Raabe, C.C. Tasan, *Nature* 534(2016) 227–230.
4. S. S. Nene, K. Liu, M. Frank, R.S. Mishra, R. E. Brennan, K. C. Cho, Z. Li, D. Raabe, *Sci. Rep.* **7** (2017) 16167.
5. S. S. Nene, M. Frank, K. Liu, S. Sinha, R.S. Mishra, B. A. McWilliams, K. C. Cho, *Scripta Mater.* **154** (2018) 163 - 167.
6. S. S. Nene, S. Sinha, M. Frank, K. Liu, R.S. Mishra, B. A. McWilliams, K. C. Cho, *Appd. Mater. Today* **13** (2018) 198 - 206.

7. S. S. Nene M. Frank, K. Liu, S. Sinha, R.S. Mishra, B. A. McWilliams, K. C. Cho, *Scripta Mater.* **166** (2019) 168 -172.
8. S. S. Nene M. Frank, P. Agrawal, S. Sinha, K. Liu, S. Shukla, R. S. Mishra, B. A. McWilliams, K. C. Cho, *Mater. Des.* **194** (2020) 108968.
9. B.H. Toby, R.B. Von Dreele, J. Appl. Cryst. **46** (2013) 544-549.
10. C. Herrera, D. Ponge, D. Raabe, *Acta Mater.* **59** (2011) 4653-4664.
11. M. Frank, S. S. Nene, Y. Chen, B. Gwalani, E. J. Kautz, A. Devaraj, K. An, R. S. Mishra, *Mater. Today Comm.* **23** (2020) 100858.
12. Y. Bu, Z. Li, J. Liu, H.Wang, D. Raabe,W. Yang, *Phy. Rev. Let.* **122** (2019) 075502.
13. L. Lu, X. Chen, X. Huang, K. Lu, *Science*, **323** (2009) 607-609.
14. S. Sinha, S.S. Nene, M. Frank, K. Liu, R. Lebensohn, R.S. Mishra,, *Acta Mater.* **184** (2020) 164-178.
15. Y. Estrin, S.S. Nene, B.P. Kashyap, N. Prabhu, T. Al-Samman, *Mater. Let.* **173** (2016) 252-256.
16. S. Sinha, N.P. Gurao, *Mater. Des* **116** (2017) 686-693.
17. E. O. Hall, *Proc. Phys. Soc. London Ser. B* **64** (1951) 747.
18. N. J. Petch, *J. Iron Steel Inst.* **174** (1953) 25.
19. M. Dao, L. Lu, Y. Shen, S. Suresh, Strength, *Acta Mater.* **54** (2006) 5421.
20. R.S. Mishra, R.S. Haridas, P. Agrawal, *Mater. Sci. Eng., A* **812** (2021) 141085.
21. Z. Li, C.C. Tasan, H. Springer, B. Gault, D. Raabe, *Sci. Rep.* **7** (2017) 40704.
22. B.B. He, B. Hu, H.W. Yen, G.J. Cheng, Z.K.Wang, H.W. Luo, M.X. Huang, *Science* **357** (2017) 1029 – 1032.
23. C. Zhang, C. Zhua, T. Harrington, K. Vecchio, *Scripta Mater.* **154** (2018) 78–82.
24. C. Zhang, C. Zhua, T. Harrington, K. Vecchio, *Mater. Sci. Eng., A* **743** (2019) 361–371.
25. Z. Ma *et al., J. Alloys Compd.* **817** (2020) 152709.
26. Z.H. Hana, S. Liang, J. Yang, R. Weid, C.J. Zhang, *Mater. Charac.* **145** (2018) 619–626.
27. Z. Fu *et al., Mater. Res. Let.* **6** (2018) 634-640.
28. K. Minga, X. Bi, J. Wang, *Intl. J. Plasticity* **113** (2019) 255–268.
29. W. Guo, J. Su, W. Lu, C. H. Liebscher, C. Kirchlechner, Y. Ikeda, F. Körmann, X. Liu , Y. Xue, G. Dehm, *Acta Mater.* **185**, 45–54 (2020).
30. L. Jiang, D. Qiao, Z. Cao, C. Lu, M. Song, L. Wang, *Mater. Sci. Eng., A* **776** (2020) 139027.

31. I. Moravcik, H. Hadraba, L. Li, I. Dlouhy, D. Raabe, Z. Li, *Scripta Mater.* **178** (2020) 391-397.
32. U. Sunkari, S.R. Reddy, S. Chatterjee, *Mater. Let.* **248** (2019) 119–122.
33. F. Zheng, G. Zhang, X. Chen, X. Yang, Z. Yang, Y. Li, J. Li, *Mater. Sci. Eng., A* **774** (2020) 138940.
34. X. Gao, Y. Lu, B. Zhang, N. Liang, G. Wu, G. Sha, J. Liu, Y. Zhao *Acta Mater.* **141** (2017) 59 - 66.
35. S.W. Wu, G. Wang, Q. Wang, Y.D. Jia, J. Yi, Q.J. Zhai, J.B. Liu, B.A. Sun, H.J. Chu, J. Shen, P.K. Liaw, C.T. Liu, T.Y. Zhang., *Acta Mater.* **165** (2019) 444 - 458.
36. P. Sathiyamoorthi, J. M. Parka, J. Moona, J. W. Bae, P. Asghari-Rad, A. Zargaran, H. S. Kim, *Materialia* **8** (2019) 100442
37. Z. Li, *Acta Mater.* **164** (2019) 400 - 412.
38. T. Yang, Y.L. Zhao, J.H. Luan, B. Han, J. Wei, J.J. Kai, C.T. Liu, *Scripta Mater.* **164** (2019) 30-35.
39. D. Wei, X. Li, W. Heng, Y. Koizumi, F. He, W. Choi, B. Lee, H.S. Kim, H. Kato, A. Chiba, *Mater. Res. Let.* **7** (2019) 82-87.
40. Z. Lei, X. Liu, Y. Wu, H. Wang, S. Jiang, S. Wang, X. Hui, Y. Wu, B. Gault, P. Kontis, D. Raabe, L. Gu, Q. Zhang, H. Chen, H. Wang, J. Liu, K. An, Q. Zeng, T. Nieh, Z. Lu, *Nature* **563** (2018) 546 - 550.
41. Z. Wang, W. Lu, H. Zhao, C. H. Liebscher, J. He, D. Ponge, D. Raabe, Z. Li, *Science Advs.* **6** (2020) eaba9543.

High strength-ductility synergy in massively interfaced Cu-HEA after conventional processing

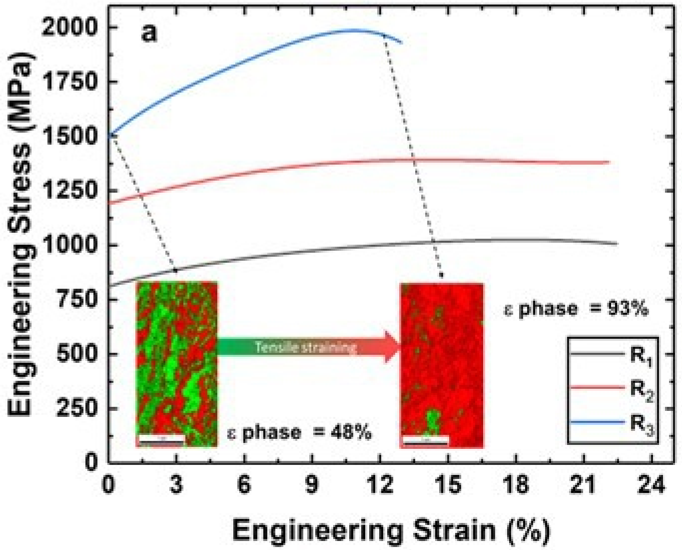

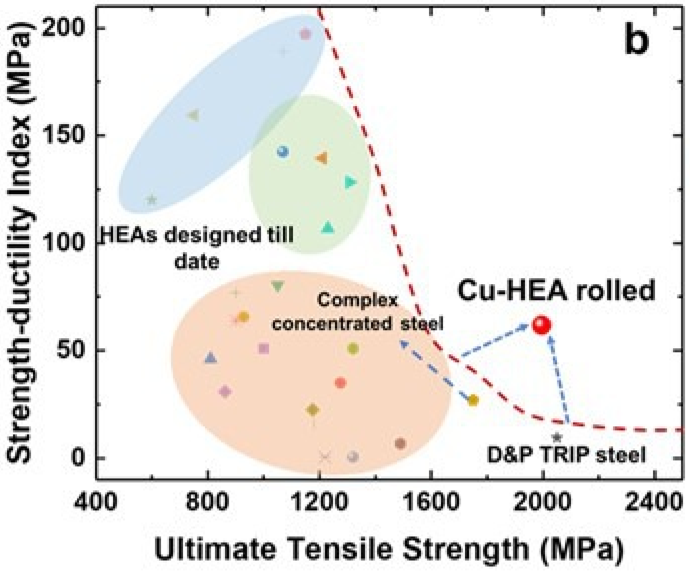

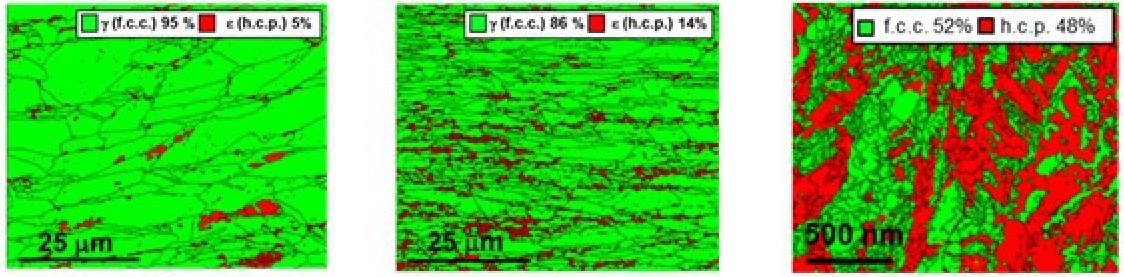

R_1 R_2 R_3

Increase in massive interfaces

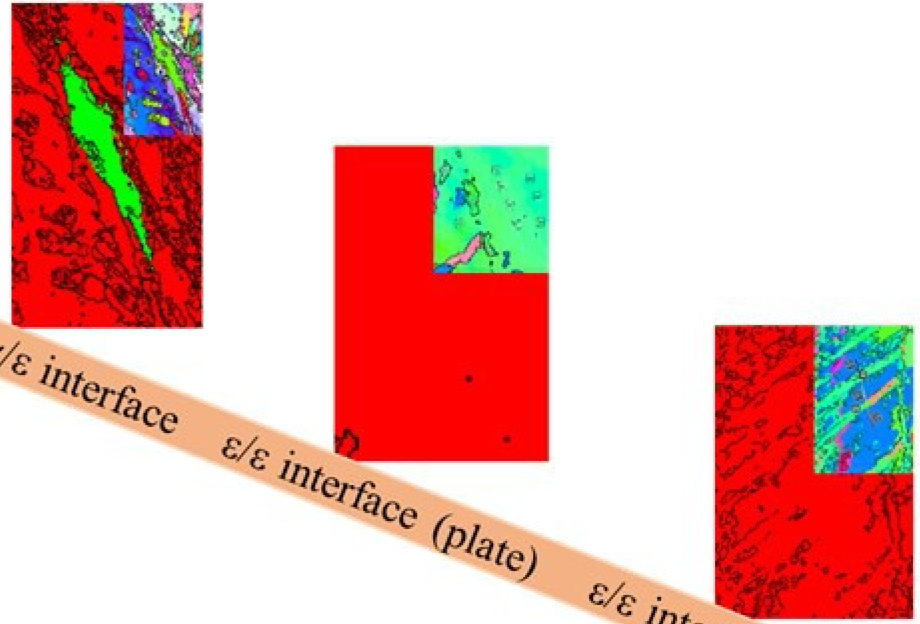

γ/ε interface ε/ε interface (plate) ε/ε interface (twins)